Volume 1 | Number 1 | Jan 2013 | Pages 1–100

Journal of
Materials Chemistry A

Materials for energy and sustainability
www.rsc.org/materialsA

Li⁺

ROYAL SOCIETY OF CHEMISTRY

ROYAL SOCIETY OF CHEMISTRY

www.rsc.org/materialsA

ARTICLE TYPE

Fabrication of MMMs with improved gas separation properties using externally-functionalized MOF particles

Surendar R Venna[a,b], Michael Lartey[a,f], Tao Li[c], Alex Spore,[c] Santosh Kumar,[a,f] Hunaid B Nulwala,[a,d] David R Luebke,[a] Nathaniel L Rosi,[c,]* Erik Albenze,[a,e,]*

Mixed matrix membranes (MMM) have the potential to overcome the limitations of traditional polymeric membranes for gas separation by improving both the permeability and selectivity. The most difficult challenge is accessing defect free and optimized MMM membranes. Defects are generally due to
10 incompatible interfaces between the polymer and the filler particle. Herein, we present a new approach to modify and optimize the surface of UiO-66-NH$_2$ based MOF particles to improve its interaction with Matrimid® polymer. A series of surface modified UiO-66-NH$_2$ particles were synthesized and characterized using ^{1}H NMR spectroscopy, mass spectrometry, XPS, and powder X-Ray diffraction. MMMs containing surface optimized MOF particles exhibit improved thermal and mechanical properties.
15 Most importantly, the MMMs show significantly enhanced gas separation properties; CO$_2$ permeability was increased by ~200% and CO$_2$/N$_2$ ideal selectivity was increased by ~25%. These results confirm the success of the proposed technique to mitigate defective MOF/Matrimid® interfaces.

1. Introduction

Membranes are a promising area of research for energy-
20 related gas separations such as CO$_2$ removal from flue or fuel gas streams as well as natural gas sweetening.[1] Polymeric membranes are cost effective and widely used for gas separation due to the ease of processing.[1] However, in polymeric membranes there is a tradeoff between improving selectivity and
25 permeability.[2,3] This tradeoff manifests itself in the Robeson upper bound which establishes upper limit combinations of permeability and selectivity for the best performing membranes. At the upper bound, an increase in permeability is met with a decrease in selectivity. Conversely, inorganic membranes have
30 perm-selectivities that are many times higher than traditional polymeric materials but are not economically feasible for large-scale applications. Most ceramic, glass, and zeolitic membrane materials exhibit costs which are orders of magnitude higher per unit of membrane area when compared to polymeric membranes.
35 Furthermore, inorganic membranes are extremely difficult to fabricate into large, defect-free areas.[4] Additionally, low surface area/unit volume, reproducibility, and long term stability of inorganic membranes remains a challenge.[5] A promising route to enhance gas transport properties and fabricate membranes
40 which exceed the Robeson upper bound involves forming composite membranes between polymeric materials and inorganic filler particles yielding mixed matrix membranes (MMM). In theory, the advantages of both the polymer (ease of processing, low cost) and the inorganic material (favorable
45 separation properties) can be realized in a MMM. MMMs have already shown promising results for applications such as flue gas purification,[6] water separation,[7,8] natural gas separation,[9] and petrochemical separation.[10]

MMMs traditionally employ rigid hydrophilic zeolites[11] or
50 carbon molecular sieve particles[12] as the inorganic filler phase, which are usually not compatible with glassy polymers. This incompatibility of surfaces results in defective polymer/filler interfaces. Moore and Koros have summarized the different non-ideal structures in MMMs such as interface voids or sieve-in-a-
55 cage, rigidified polymer layer around the inorganic fillers, and particle pore blockage.[13] In order to surpass the Robeson upper bound, the structure of the MMM has to be defect-free at the polymer/filler interface. This ideal morphology is difficult to achieve due to poor polymer/filler adhesion.[14–16] Overcoming
60 poor adhesion requires careful selection of a filler and polymer which are likely to interact well. However, this limits the selection of polymers and fillers to only those that are likely to form a defect-free interface.

Metal-organic frameworks (MOFs) are a relatively new
65 class of porous materials which show promise as adsorbents and membranes for gas separation applications.[17–19] MOFs are periodic structures that consist of metal ions or clusters interconnected by organic linkers. Their structures are highly tailorable: by varying the organic linker and/or metal ion, one
70 can introduce new functionality, adjust the pore size, and tune the chemical properties and gas transport properties to a specific application.[20–24] As a result of their organic/inorganic hybrid structure, MOFs are intrinsically more compatible with polymers and show greater promise as filler materials in MMMs compared
75 to other inorganic materials.[6,10,14,25–31] Several different MOFs were used to fabricate MMMs such as Cu$_3$BTC$_2$,[25] ZIF-8,[28] MOF-5[29] and MIL-53.[30] HKUST-1 and ZIF-8 were also used in combination with Silicalite-1 zeolites to prepare MMMs by dispersing in polysulfone polymer.[32]
80 This study focuses on the development of a technique to control and optimize the interactions between the polymer and the porous filler particles, thereby improving the mechanical and

gas separation properties of the MMMs. The application under consideration is post-combustion carbon capture, namely, the separation of CO_2 and N_2. The specific technique reported here involves surface functionalization of MOF particles to ensure optimized interaction with the polymer. Using this approach, the structure of the polymer is analyzed to determine functional groups that are likely to form an ideal interface between the polymer and the MOF. The potential organic moieties are then chemically linked to the surface of the MOF particle. To accomplish this, MMMs were developed using UiO-66-NH_2 as the dispersed phase and Matrimid® as the continuous matrix. UiO-66-NH_2[33] was chosen as the MOF filler material because i) the Lewis-basic amino groups not only convey selective adsorption of CO_2 but also they can be post-synthetically modified, allowing introduction of chemical moieties that interact well with the polymer matrix and ii) compared to many other MOFs, UiO-66-NH_2 has high water, chemical, and thermal stability.[34–39] The UiO-66-NH_2 structure consists of $Zr_6O_4(OH)_4$ clusters bridged together by 12 2-amino-1,4-benzenedicarboxylate (NH_2-BDC) linkers. It is permanently porous, and cavities within the structure are accessible through ~0.6 nm triangular windows.[33,40] Matrimid® was selected as the polymer for this study because it is well-characterized glassy polymer. Since the incorporation of fillers into a glassy polymer like Matrimid® has proven difficult because of material incompatibility and rigid chain mobility,[13,41,42] Matrimid® is an excellent choice for this study because a technique that is successful on a glassy polymer like Matrimid® is likely to be successful on rubbery polymers and other low glass transition temperature polymers. Four MOFs having polar, non-polar, or aromatic surface functional groups are compared to probe the effectiveness of this approach: neat UiO-66-NH_2 (**I**), aromatic-modified **I** (**I_{PA}**), aliphatic C_{10}-modified **I** (**I_{C10}**), and acid-modified **I** (**I_{SA}**).

2. Experimental Section

2.1. Materials synthesis and membrane fabrication

Matrimid® 5218 polymer was obtained from Huntsman Chemical. All other chemicals were purchased from Sigma Aldrich Chemical and were used as received without any further purification.

UiO-66-NH_2 synthesis and post synthetic modification

UiO-66-NH_2 (I): The synthesis was adapted from reported syntheses.[33,38,43] Stock solutions of $ZrCl_4$ (0.1 M), 2-aminoterephthalic acid (0.1 M), and HCl (conc.) (1 M) in DMF were first prepared. To a 40 ml vial were added 10 mL $ZrCl_4$ (1 mmol), 20 mL 2-aminoterephthalic acid (2 mmol), and 3 mL HCl (3 mmol). The vial was capped and heated in a 120°C oven for 24 hours. Yellow microcrystalline product was centrifuged (5 min, ~1000 rpm) and washed first with DMF (3X) and then with $CHCl_3$ (3X). The product was then dried in a 130°C oven (24 h), collected, and stored in a capped vial and used for subsequent functionalization steps without further purification.

Modification of I with Phenyl Acetyl Group (I_{PA}): **I** (2.0 g, 0.63 mmol) was suspended in $CHCl_3$ (20 mL) in a 40 mL vial. While stirring, phenylacetyl chloride (1.5 mL, 11.4 mmol) and triethylamine (1.4 mL, 10 mmol) were added and the resulting mixture was allowed to stir at room temperature (16 h). The yellow product was centrifuged (5 min, ~1000 rpm), washed with chloroform (3X), and dried in a 130°C oven (16 h). The product was stored in a capped vial.

Modification of I with Decanoyl Acetyl Group (I_{C10}): **I** (2.0 g, 0.63 mmol) was suspended in $CHCl_3$ (20 mL) in a 40 mL vial. While stirring, decanoyl chloride (2.4 mL, 11.4 mmol) and triethylamine (1.4 mL, 10 mmol) were added and the resulting mixture was allowed to stir at room temperature (16 h). The yellow product was centrifuged (5 min, ~1000 rpm), washed with $CHCl_3$ (3X), and dried in a 130°C oven (16 h). The product was stored in a capped vial.

Modification of I with Succinic Acid Group (I_{SA}): **I** (2.0 g, 0.64 mmol) was placed in dry DMF (20 mL) with 3Å molecular sieves (~5-10 sieves dried for 2d at 200°C and then evacuated prior to use). While stirring, succinic anhydride (2.0 g, 19.9 mmol) was added and the mixture was heated in a 60°C oil bath (16 h). The yellow product was centrifuged (5 min, ~1000 rpm), washed with DMF (3X), washed with $CHCl_3$ (3X), and then dried in a 130°C oven (16 h). The product was stored in a capped vial.

Membrane fabrication

For preparation of the neat Matrimid® dense membrane, Matrimid® was dried in a vacuum oven at 120°C overnight. Next, a dope solution was formed by dissolving the Matrimid® in chloroform followed by mixing on a roller mixer. Then, the dope was kept stationary overnight to remove any retained gas bubbles. Prior to casting, a glove bag was purged with N_2 to remove any humidity and was saturated with chloroform to slow the rate of solvent evaporation from the membrane. Matrimid® dense membranes were cast onto a glass plate in the glove bag using a casting knife. The resulting membrane was kept for 2 days in the glove bag as the chloroform evaporated slowly from the membrane. The membrane was dried at 100°C overnight followed by annealing at 225°C in a vacuum oven for 2 hours. Finally, the membrane was slowly cooled to room temperature. To ensure full activation of the MOF, Soxhlet-extraction was employed to extract residual DMF from the MOF framework. The sample was loaded in the Soxhlet extraction apparatus and extracted for 7 days, using dichloromethane as the extracting agent. For preparation of the MMMs, both the Matrimid® and MOF were dried in a vacuum oven at 120°C overnight. Preparation of the dope solution followed the standard 'priming' technique in which the MOF particles were first dispersed in chloroform solvent using an ultrasonication water bath for 2 hours to obtain a homogenous dispersion. Next, the MOF crystals were primed by adding 30% of the total Matrimid® to the MOF/chloroform solution followed by roller mixing and sonication for another 2 hours. The remaining Matrimid® polymer was added in two steps (30% and 40%) followed by stirring and sonication after each addition. The mixed matrix dense films were formed by casting the mixed matrix dope as discussed above for the neat Matrimid® membranes. The MOF loading was controlled by changing the mass ratio of MOF to Matrimid® in the mixed matrix dope solution. MMMs with low (12 wt%), medium (23 wt%), and high (40 wt%) loadings of MOF were fabricated using **I** (MMM-I) and **I_{PA}** (MMM-I_{PA}). MMMs were also prepared using 23 wt% **I_{SA}** (MMM-I_{SA}) and 23 wt% **I_{C10}** (MMM-I_{C10}) to study the effect of different surface functionalizations on the Matrimid®/MOF filler adhesion and the gas separation performance. The loadings represented here – 12 wt%, 23 wt%, and 40 wt% – correspond to volume percentages of approximately 11%, 22% and 38%, respectively.

2.2. Characterization

MOF Structure: Powder X-Ray diffraction (PXRD) was used to verify the phase purity and homogeneity of the MOF samples. Each pattern was collected using a Bruker AXS D8 Discover powder diffractometer at 40 kV, 40 mA for Cu Kα, (λ = 1.5406 Å) with a scan speed of 0.20 sec/step and a step size of 0.02018°. The simulated powder pattern was calculated using Mercury 2.4 software.

MOF Composition: Liquid chromatography-mass spectrometry (LCMS) was used to confirm that **I** was successfully functionalized to yield I_{PA}, I_{C10}, or I_{SA} (**Figures S1-S3**). For LCMS, ~5 mg of MOF sample was digested in a solution of MeOH/HF/H_2O (500 μL MeOH and 5 μL of 48% HF in H_2O). The mixture was shaken to dissolve the MOF. Analyses were performed on a Shimadzu LCMS-2020. LC methods were employed using an acetonitrile/water eluent. The flow rate was held steady at 0.2 mL/min and acetonitrile was increased steadily from 10 % to 90 % over 0-9 min and then reduced to 10% acetonitrile for the final minute. The ionization interface was simultaneous ESI & APCI.

^{1}H NMR spectroscopy was used to estimate the degree of functionalization of the post-synthetically modified MOFs. For these studies, ~5mg of MOF sample was digested in a solution of d4-MeOD/HF/H_2O (500 μL d4-MeOD and 5 μL of 48% HF in H_2O). The mixture was shaken to dissolve the MOF. Spectra of dissolved MOFs were collected at room temperature using Bruker Avance 300 MHz spectrometers. The integration for each proton of the H_2-NH_2-BDC ligand was set at 1. Chemical shifts are in parts per million using the residual solvent peak as the reference value. The values used for proton spectra, respectively, are 3.3 ppm for d-MeOH.

X-ray photoelectron spectroscopy (XPS) measurement was carried out with a PHI 5600ci instrument using monochromatic Al Kα x-rays. The pass energy of the analyzer was 58.7 eV. The relative amounts of different chemical states of carbon were determined by curve fitting the C 1s spectra using Casa XPS software. A peak at 284.6 eV was used as the binding energy reference and was assigned to C-C and C=C functionalities. A peak at 285.8 eV was assigned to C-O and C-N functionalities, and a peak at 288.6 eV was assigned to carboxyl carbon.

Gas adsorption: Gas adsorption isotherms were collected volumetrically as a function of relative pressure using an Autosorb 1 from Quantachrome. Activated MOF samples were weighed using an AB54-S/FACT (Mettler Toledo) electrogravimetric balance (sensitivity 0.1 mg). 9 mm large bulb cells (from Quantachrome) of a known weight were loaded with ~60 mg of sample for gas adsorption experiments. The samples were degassed at 150°C for 12-24 hours on the degassing station until the outgas rate was no more than 3.0 mTorr/min. The degassed sample and sample cell were weighed precisely and then transferred back to the analyzer. The temperature of each sample for N_2 adsorption experiments was controlled using a refrigerated bath of liquid nitrogen (77 K). CO_2 and N_2 isotherms (273 K and 298 K) were measured in a temperature-controlled water bath. The N_2 and CO_2 adsorbates were of UHP grade.

Thermal Analysis: Thermogravimetric analysis (TGA) of each MOF sample was performed using a TGA Q500 thermal analysis system. All TGA experiments of MOF samples were performed under a N_2 atmosphere from 25-600°C at a rate of 5°C /min. TGA was also used to determine the thermal stability of the MMMs and to analyze any remaining solvent in the membranes. The MMM samples were first heated up to 100°C and kept at 100°C for 15 min under N_2 atmosphere in order to remove the adsorbed water. The samples were then cooled down to 50°C and the temperature was subsequently increased to 700°C at a rate of 10°C/min. The glass transition temperature (Tg) for each membrane was determined using a differential scanning calorimeter (Q2000, TA Instruments). The measurement was carried out using a standard heating-cooling-heating procedure at heating/cooling rates of 10 K/min in a nitrogen atmosphere.

Microscopy: Scanning electron microscopy (SEM) was performed on an FEI Quanta 600 scanning electron microscope to determine the particle size of the MOF crystallites, as well as to evaluate the cross sectional structure of the fabricated membranes. The membrane samples were prepared by fracturing the membranes in liquid nitrogen and subsequent sputter coating of palladium using a SPI Module Sputter Coater.

Mechanical Studies: The mechanical strength of the membranes with different MOF loadings was studied at 30°C using a dynamic mechanical analyzer (Q800, TA Instruments). Testing was performed in triplicate.

Gas separation performance measurement: The pure gas CO_2 and N_2 permeation tests were performed at room temperature using an isochoric (constant volume, variable pressure) permeation system. Upstream pressures were measured with a pressure transducer (Maximum pressure 150 psia, Viatran Inc., Model-345) and accompanying readout (Dalec Electronics digital panel). Downstream pressures were measured using a Baratron 627D capacitance manometer with a maximum pressure output of 10 Torr (MKS, Wilmington, MA). The downstream volume was calibrated by using a standard simple mole balance method with a known volume of stainless steel balls. Membranes coupons were formed using a hole punch resulting in a membrane of diameter 2.5 cm. The thicknesses of the membranes were measured using a micrometer (Marathon Electronic digital micrometer) several times and the average value was used for the calculation of permeability.

Testing was carried out as follows: the membrane was loaded into a Millipore high pressure 25 mm filter holder resulting in an exposed area for transport of 2.7 cm^2. The entire permeation system was degassed using a vacuum pump (Edwards nXDS 10i scroll pump) for 18 hours and then the leak rate was measured by isolating the permeation system from the vacuum pump. The leak rate was always much less than the typical steady state pressure rise during gas permeation measurement (as shown in Figure S22). The feed gas was then introduced to the upstream side of the membrane, and the pressure rise in the downstream volume was recorded as a function of time. Two film samples were tested at each MOF loading to get average permeation results. CO_2 and N_2 gas downstream pressure rise rates of all the membranes tested in the isochoric system are shown in the supporting information (Figures S23 –S25).

The permeation of a gas through the membrane can be described using the solution-diffusion model. The permeability of a gas, i, is given by: $P_i = D_i \cdot S_i$, where D_i and S_i represent the diffusion and solubility coefficients of component i, respectively. In terms of this model, the productivity of a membrane is defined by the permeability of the gas through the membrane and the selectivity of the membrane is the ratio of the permeabilities of the individual gases. Permeability was calculated by differentiating the pressure rise as a function of time and using the following equation:

$$P = \frac{V_d l}{p_2 ART}\left[\left(\frac{dp_1}{dt}\right)_{ss} - \left(\frac{dp_1}{dt}\right)_{leak}\right]$$

Where, V_d = downstream volume (cm^3), l = film thickness (cm), p_2 = upstream absolute pressure (cmHg), A = film area (cm^2), T = Temperature (K), R = gas constant (cm^3 cmHg/mol K), $(dp_1/dt)_{ss}$ = rate of downstream pressure rise during testing (cmHg/sec), $(dp_1/dt)_{leak}$ = rate of downstream pressure rise under vaccum (cmHg/sec). It is important to note that there is a difference between the ideal selectivity of a membrane defined as the ratio of individual permeabilities of the gases during separate pure gas testing and the real selectivity of a membrane defined as the ratio of the individual permeabilities during a test using a mixture of both gases. All testing performed here was pure gas testing, therefore all selectivities are ideal.

3. Results and Discussion

3.1. UiO-66-NH$_2$ and surface-functionalized UiO-66-NH$_2$

5 **I** was modified with a phenyl acetyl group (PA), a decanoyl acetyl group (C$_{10}$), or a succinic acid group (SA) (Scheme 1) using straightforward acyl chloride-amine condensation or acid-amine condensation reactions. Powder X-Ray diffraction (PXRD) patterns of **I** before and after functionalization are shown 10 in Figure 1A. The diffraction lines are in good agreement with the simulated XRD pattern, confirming formation of the pure phase crystalline **I**. PXRD patterns of **I$_{PA}$**, **I$_{SA}$**, and **I$_{C10}$** were also consistent with the pattern of **I**, confirming that the crystallinity was maintained even after functionalization. SEM images of each 15 of the MOF analogues were used to determine the average particle size. The average particle size of all these MOF analogues was ~200 nm and aggregation was observed. An SEM image of **I$_{PA}$** particles is shown in Figure 1B as an example; no changes in the particle morphology were observed after the 20 modification.
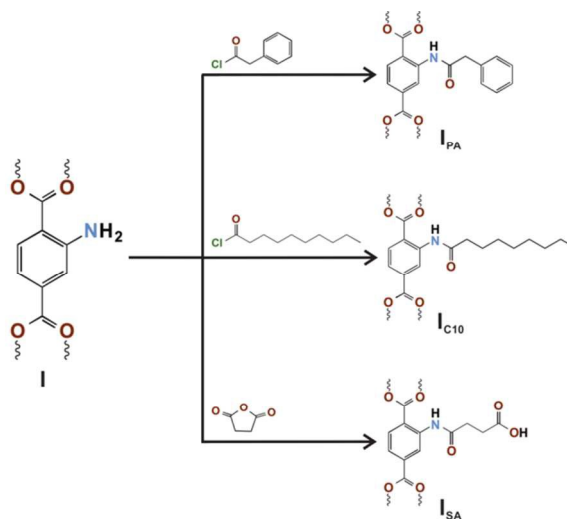
Scheme 1. Post-synthetic modification of UiO-66-NH$_2$ (**I**) for functionalization of the NH$_2$-BDC ligand.

25

The composition of **I$_{PA}$**, **I$_{SA}$**, and **I$_{C10}$** was determined by collecting LCMS, XPS and ^{1}H NMR spectra for digested MOF samples. Data analysis details are included in the Supporting Information. Briefly, LCMS studies (Figures S1-S3) confirmed 30 the presence of both functionalized and unfunctionalized ligand for **I$_{PA}$**, **I$_{SA}$**, and **I$_{C10}$**. ^{1}H NMR (Figures S4-S7 and Tables S1-S4) was used to determine the ratio between unfunctionalized and functionalized ligand for **I$_{PA}$**, **I$_{SA}$**, and **I$_{C10}$**. The percentage of functionalized ligands was found to be between 2-6% for **I$_{PA}$**, 2-35 5% for **I$_{C10}$**, and 16-32% for **I$_{SA}$**. We expect that, for **I$_{PA}$** and **I$_{C10}$**, the phenyl substituents and C$_{10}$ chains are located on the external surface of the MOF particles, because functionalization at internal amino sites would be significantly limited by diffusion of the large phenyl and C$_{10}$ reactants. XPS analysis of the 40 functionalized MOFs before and after crushing also indicated that the organic ligand functionalization was likely predominantly on the external surface of the MOF particles (Figure S8-S9). The observed BET surface areas for **I$_{PA}$** and **I$_{C10}$** are similar to that for **I** (vide infra), which is consistent with this interpretation. It is 45 clear from our results that the SA groups react significantly with internal amino sites, because 16-32% of the ligands are

functionalized with SA. SA is smaller than phenylacyl chloride and decanoyl chloride, and its reaction with the internal amino groups would not be nearly as diffusion limited. The BET 50 surface area for **I$_{SA}$** is significantly lower than **I** (vide infra), which, again, is consistent with the observed degree of functionalization.
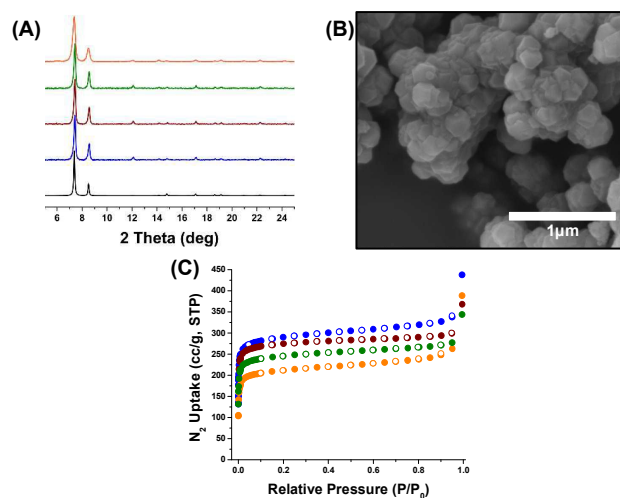
55

Figure 1. PXRD patterns (A), sample SEM image (**I$_{PA}$**) (B), and N$_2$ isotherms at 77K (C) for **I** (blue), **I$_{PA}$** (green), **I$_{C10}$** (maroon) and **I$_{SA}$** (orange).

60 The N$_2$ isotherms collected at 77K for **I**, **I$_{PA}$**, **I$_{SA}$**, and **I$_{C10}$** are shown in Figure 1C. Type I isotherms were observed confirming the microporous nature of the materials. The apparent surface area of **I** was 1135 m^2/g, which is similar to previous reports.[33] The BET surface areas of **I$_{PA}$** and **I$_{C10}$** were each 65 slightly lower than **I** (962 m^2/g for **I$_{PA}$** and 1079 m^2/g for **I$_{C10}$**) while that for **I$_{SA}$**, 827 m^2/g, was significantly lower than **I**, for reasons described above. The BET surface areas for the functionalized analogues indicate that these samples have accessible internal surface, and they are consistent with the 70 observed degree of functionalization for each of these samples. CO$_2$ isotherms for each sample were collected at 273 K and 298 K (Figures S12 and S14). The amount of CO$_2$ adsorbed at 273 K and 298 K for each material corresponds closely to the observed BET surface areas for these materials; that is, the larger the BET 75 surface area, the larger amount of CO$_2$ adsorbed at 1 bar.

3.2. Matrimid® and MMM characterization

Neat dense Matrimid® membranes and Matrimid®/MOF MMMs were prepared and analyzed using PXRD. The XRD 80 patterns were used to confirm the presence of UiO-66-NH$_2$ analogues in the MMMs as shown in Figure 2. The most evident diffraction lines observed for the MMMs match those for the neat MOFs, which confirms the preservation of the crystal structure after incorporation of the MOF particles in the Matrimid® 85 polymer matrix.

Thermograms obtained for **I**, **I$_{PA}$**, **I$_{C10}$**, and **I$_{SA}$** after Soxhlet extraction are shown in Figure 3A. The initial weight loss observed for all of the MOF samples is attributed to adsorbed water, because UiO-66-NH$_2$ is hygroscopic. The weight loss 90 around 200-300°C is attributed to residual DMF in the pores. The observed weight loss at higher temperatures corresponds to the decomposition of the ligand. The neat Matrimid® and MMM films were also studied using TGA to determine the effect of the MOF particles on the thermal stability of the membranes. The

weight loss as a function of temperature is shown in Figures 3B-D. The thermal decomposition of neat Matrimid® begins around 440°C. Overall, thermogravimetric analyses of the MMMs showed minimal weight loss up to 300°C indicating that the casting solvent was not trapped in the pores of the MOF.
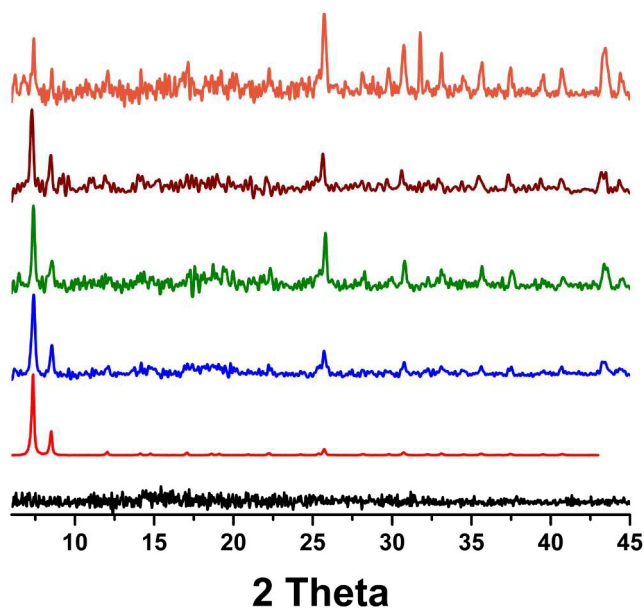

Figure 2. PXRD patterns for Matrimid® (black), **I** (red), MMM containing **I** (blue), MMM containing **I$_{PA}$** (green), MMM containing **I$_{C10}$** (maroon), and MMM containing **I$_{SA}$** (orange) confirm the existence of MOFs within the MMMs.
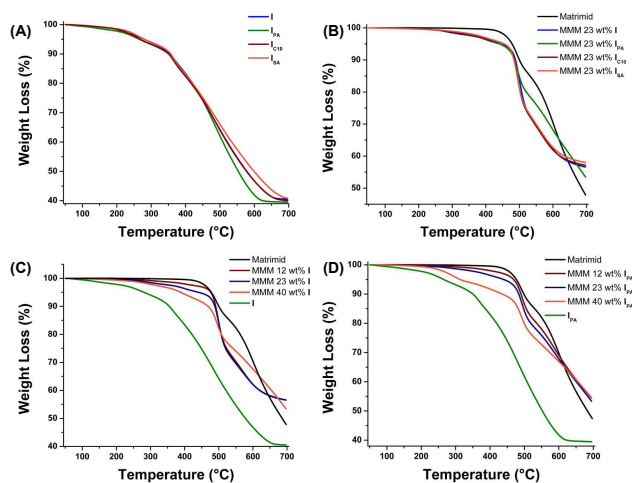
Figure 3. Thermogravametric analysis of MOF analogues (A), 23 wt% loaded MMMs (B), MMMs containing varying amounts of **I** (C), and MMMs containing varying amounts of **I$_{PA}$** (D).

The decomposition of MMMs with a moderate loading of 23 wt% MOF is shown in Figure 3B. The thermograms are very similar, indicating that the surface functionalization of **I** has minimal effect on the decomposition of the MMM. This is in agreement with the results for the neat MOFs (Figure 3A). Figures 3C and 3D show the effect of loading on the decomposition temperature of the MMMs. For both cases, **I** and **I$_{PA}$**, the decomposition temperature of the MMM decreased with increased loading. Usually the decomposition temperature of a MMM increases with an increase in the MOF loading because the interaction between the Matrimid® and MOF particle restricts the

thermal motion of polymer. This restricted motion increases the energy needed for the movement and segmentation of polymer chains, which enhances the thermal stability of the membranes.[44] The results presented here show the opposite trend of a decreasing decomposition temperature with increased loading. This trend occurs because the decomposition temperature of the MOF is substantially lower (by more than 100 °C) than that of the Matrimid®. The decomposition of the MOF analogues in the MMMs begins at ~300°C, much earlier than Matrimid®. Similar trends were reported for $Cu_3(BTC)_2$ MOF based MMMs.[25]

SEM was used to study the membrane cross section morphology as well as to image the particle-polymer interface. Figure 4A shows an SEM image of a cross-section of a neat Matrimid® membrane. Its surface is very smooth without any noticeable defects, which is characteristic of a dense Matrimid® membrane. Representative cross sectional images of the MMMs with 12, 23 and 40 wt% of **I$_{PA}$** are shown in Figures 4B, 4C, and 4D, respectively. From the images, no obvious defects around the **I$_{PA}$**, particles were observed. At low to moderate loadings (12-23 wt%) the **I$_{PA}$** particles were typically well-dispersed. However, at high loadings, several large clusters of **I$_{PA}$** particles exist. These clusters range in size from 500 nm to several microns. Aggregated clusters often contain nonselective diffusion paths between the individual crystallites which reduces the overall performance of the membrane.[45–47]
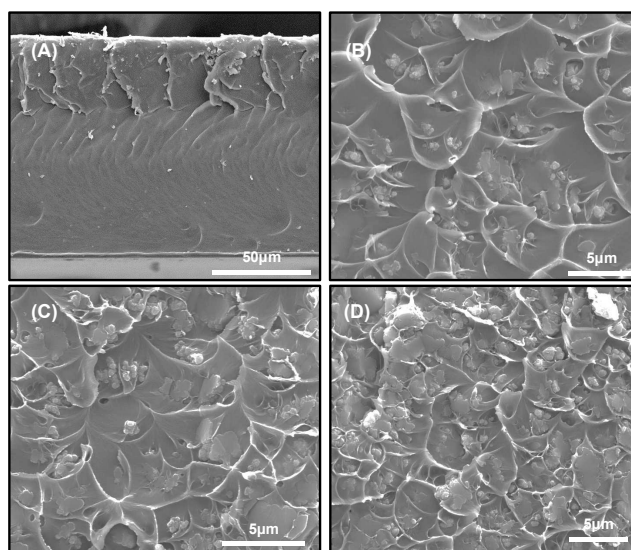

Figure 4. SEM images for a neat Matrimid® membrane (A) and loadings of 12 wt% (B), 23 wt% (C), and 40 wt% (D) of **I$_{PA}$** in Matrimid®.

A second important feature of the SEM micrographs is the scalloped morphology observable for the MMMs that is not present for the neat Matrimid® membrane. This morphology is typically attributed to the formation of elongated polymer segments with increased plastic deformation of the polymer, and is taken as an indication that there is good interaction between the polymer and filler.[28,29,48,49] The absence of any observable sieve-in-a-cage morphology or cavity formation at each loading is an indication of good film formation and strong interaction between the Matrimid® and **I$_{PA}$** particles. There was no easily observable difference between the cross sectional images of **I**, **I$_{PA}$**, **I$_{C10}$**, and **I$_{SA}$** loaded MMMs (Figure S21). More sophisticated techniques like nano-computed tomography scanning (nano-CT), positron annihilation lifetime spectroscopy (PALS), or FIB-SEM are

needed to detect if there are any nano-defects or rigidification of the polymer around the particle.[30,31,50]

Figure 5 shows the Young's Modulus of the pure Matrimid® and MMMs as determined by dynamic mechanical analysis (DMA). It is immediately obvious that all of the MMMs have a significantly higher modulus compared to the pure Matrimid® membrane. In addition, the Young's Modulus of the membranes increases with MOF loading from 12 wt% to 23 wt%. But at 40 wt%, the Young's Modulus decreased indicating less interfacial interaction between the polymer and MOF resulting from the aggregation of the particles as shown in Figure 4D. The significant increase in storage modulus of the MMMs indicates a good dispersion of MOF particles throughout the membrane as well as a good interaction between the MOF particle and Matrimid® polymer.
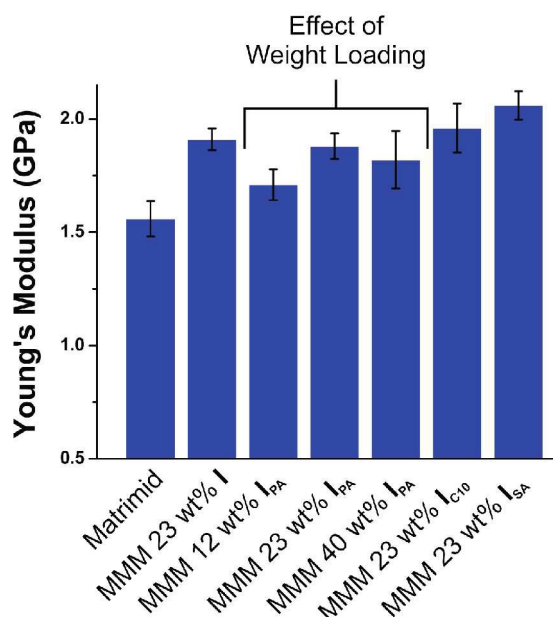
Figure 5. Young's Modulus for Matrimid® and the MMMs with different functionalities and weight loadings of I_{PA}.

Differential scanning calorimetry (DSC) was used to determine the effect of the MOF particles on the glass transition temperature (Tg) of the polymer phase (Figure S26). The measured Tg of Matrimid® was 324 °C which is in good agreement with literature.[25] An increase in the Tg of no greater than 3° was observed for all of the MMMs with an increase of 2° or less observed for all but the highest loading of I_{PA}. An increase in the Tg upon incorporation of the MOF particles is often taken as evidence of rigidificaton at the polymer/filler interface. Some rigidification is expected as a result of the interaction between the MOF particles and the Matrmid® polymer, limiting the mobility of the polymer chains adjacent to the particle. Many previous studies have reported similar increases in the glass transition temperatures upon incorporation of the filler in the matrix.[25–27] It should also be noted that the Tg for Matrimid® is greater than the decomposition temperature of the MOF analogues. As a result, the MOF particles may have started to decompose during these measurements resulting in error in the measurement.

3.3. CO_2/N_2 gas separation performance of MMMs

Pure gas CO_2 and N_2 permeation measurements of neat Matrimid® and the MMMs were completed using an isochoric

permeation system at room temperature and 20 psia upstream pressure. The results are presented in Figures 6 and 8. All membranes were tested twice to check the reproducibility and determine the percent error, which was 2-5% for both the permeability and ideal selectivity. The dense Matrimid® membrane showed a CO_2 permeability of 8.5 Barrer with a CO_2/N_2 ideal selectivity of 29, in agreement with previously reported values.[29,30]

Figure 6 presents the permeability and ideal selectivity results for the MMMs with 23 wt% loading of all four MOF analogues. In all cases, the CO_2 permeability increased dramatically compared to the value for the neat Matrimid® polymer. In fact, the CO_2 permeability increased as much as 4 times upon incorporation of the MOF particles. In addition to a substantial increase in the permeability, the MMMs with I and I_{PA} filler particles also exhibited an increase in ideal selectivity compared to the neat Matrimid® film. This improvement in ideal selectivity is attributed to the formation of a defect-free interface between the particle and polymer. Alternatively, the improved ideal selectivity may be attributed to significant rigidification of the polymer around the particle. Such rigidification would lead to increased ideal selectivity but decreased gas permeability. In the case of the Matrimid®/I and Matrimid®/I_{PA} membranes presented here, the overall permeability increased substantially indicating this scenario is unlikely. It should be noted that UiO-66-NH2 may provide minimal molecular sieving selectivity because the pore size of UiO-66-NH2 (6-7 Å) is larger than the kinetic diameter of both CO_2 (3.3 Å) and N_2 (3.64 Å). However, it is expected that UiO-66-NH2 and the analogues used here may provide selectivity towards CO_2 due to a surface diffusion mechanism since CO_2 adsorbs more favorably with the MOF compared to N_2. Overall, these results are promising, especially compared to previous MMM work with other MOFs.[26,28,30]
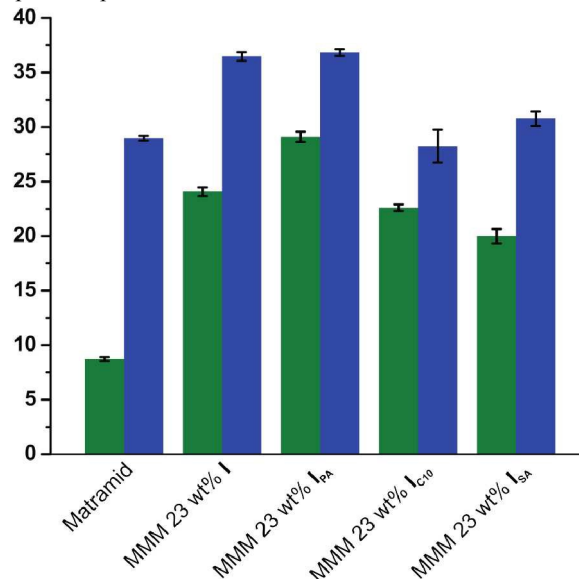

Figure 6. CO_2 permeability (green, in Barrer) and CO_2:N_2 ideal selectivity (blue) for Matrimid® as well as MMMs containing 23 wt% of the functionalized MOFs.

The transport properties for the MMMs with the I_{SA} and I_{C10} surface-functionalized MOFs are also shown in Figure 6. The I_{SA} MMMs showed only slight improvement in ideal selectivity over pure Matrimid®, while I_{C10} showed a decrease in ideal selectivity. These membranes were also the most fragile and difficult to handle, with I_{SA} yielding the most brittle membrane. The

decreased transport and mechanical properties resulting from the SA and C_{10} surface functional groups are interesting because they indicate that the MOF filler does not interact as strongly with the polymer matrix resulting in unobservable defects at the Matrimid®/MOF interface. These defects increase the brittleness of the membrane and act as non-selective alternate diffusion paths for the gases, resulting in the decreased transport performance. This decreased performance can be predicted by examining the structure of Matrimid® which contains aromatic and imide groups. The surface functional groups (SA – polar; C_{10} – non-polar alkyl) are not expected to interact well with the functional groups in the Matrimid® polymer.
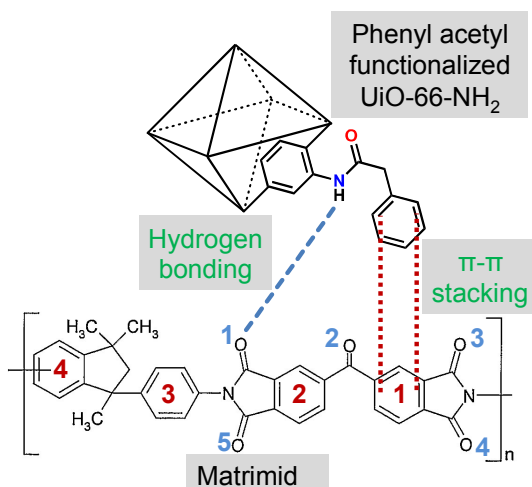
Figure 7. Scheme demonstrating the favorable interactions between the Matrimid® polymer and $\mathbf{I_{PA}}$ based on surface functionality.
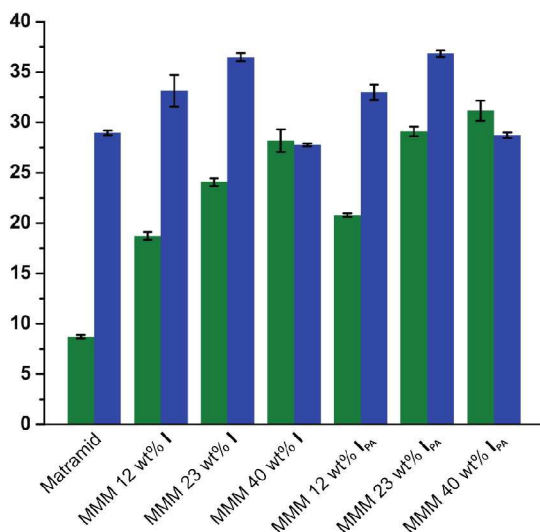

Figure 8. CO_2 permeability (green, in Barrer) and CO_2:N_2 ideal selectivity (blue) for 12, 23, and 40 wt% loadings of $\mathbf{I}$ and $\mathbf{I_{PA}}$.

Conversely, for –NH_2 and –PA surface-functionalized MOFs, the aromatic groups present in the polymer are expected to interact favorably through π-π stacking with the aromatic ring of the –PA group and the imide groups in the polymer are expected to interact strongly with the –NH_2 groups and amide linkages through hydrogen bonding as shown in Figure 7. Furthermore, since all four MOF analogues have *nearly* identical

internal structure and functionality (we note that I_{SA} has significant internal SA functionalization) and only differ by the organic moiety present at the surface, it can be concluded that simply changing the surface organic moiety can significantly affect whether the polymer/filler interface is truly defect-free.

Additional MMMs were fabricated for the two best performing MMMs, those containing $\mathbf{I}$ or $\mathbf{I_{PA}}$ MOF particles, with MOF loadings of 12 wt% and 40 wt%. The results, along with those for the 23 wt% loading, are shown in Figure 8. As expected, both the permeability and the ideal selectivity increase with loading up to 23 wt%. However, for the 40 wt% loadings, further increase in the permeability was observed, but the ideal selectivity values decreased compared to the 23 wt% loading. This is attributed to the agglomeration observed at the higher loading as shown in Figure 4D. The agglomerated clusters result in microvoids which act as non-selective diffusion pathways for the gas molecules resulting in a lower observed ideal selectivity.

4. Conclusions

The work presented here successfully demonstrated that we can control the interaction at the polymer/particle interface by functionalizing the MOF with different organic moieties. The results presented here indicate that the interaction between the MOF and polymer is in the following order: $\mathbf{I_{PA}}$>$\mathbf{I}$>$\mathbf{I_{C10}}$>$\mathbf{I_{SA}}$. By controlling the interaction at the interface, one of the major challenges with MMMs, poor interaction between the polymer and filler, can be mitigated. While similar methods have been applied in the case of zeolites through silanation of the surface, no attempt to specifically functionalize the surface of MOF particles to improve interaction with the polymer matrix has been reported. This is a significant step forward because MOF particles have distinct advantages over zeolites and other filler materials in terms of the vast number of available MOFs and their ease of tunability. The technique presented here permits surface functionalization of the MOF crystallites with a wide variety of functional groups while not altering the internal (i.e. bulk) structure of the crystallite. The end result is a robust technique for modifying a MOF to ensure good adhesion with a polymer of choice and for fabricating MMMs with improved gas separation.

Notes and references

[a] *National Energy Technology Laboratory, Pittsburgh, PA 15236*
[b] *West Virginia University Research Corporation, Morgantown, WV*
[c] *University of Pittsburgh, Pittsburgh, PA 15260*
[d] *Carnegie Mellon University, Pittsburgh, PA 15213*
[e] *URS Energy and Construction, Pittsburgh, PA 15236*
[f] *Oak Ridge Institute for Science and Education, Oak Ridge, TN 37831*

E-mail: erik.albenze@netl.doe.gov, nrosi@pitt.edu

Disclaimer
This project was funded by the Department of Energy, National Energy Technology Laboratory, an agency of the United States Government,

References

1 P. Bernardo, E. Drioli, and G. Golemme, *Ind. Eng. Chem. Res.,* 2009, **48,** 4638–4663.

2 B. D. Freeman, *Macromolecules,* 1999, **32,** 375–380.

3 L. M. Robeson, *J. Memb. Sci.,* 2008, **320,** 390–400.

4 S. R. Venna and M. A. Carreon, *Langmuir,* 2011, **27,** 2888–2894.

5 L. C. A.J. Burggraaf, *Fundamentals of Inorganic Membrane Science and Technology*, Elsevier, 1996.

6 Y. Dai, J. R. Johnson, O. Karvan, D. S. Sholl, and W. J. Koros, *J. Memb. Sci.,* 2012, **401,** 76–82.

7 O. Bakhtiari, S. Mosleh, T. Khosravi, and T. Mohammadi, *Desalin. Water Treat.,* 2012, **41,** 45–52.

8 L. M. Vane, V. V. Namboodiri, and T. C. Bowen, *J. Memb. Sci.,* 2008, **308,** 230–241.

9 A. M. W. Hillock, S. J. Miller, and W. J. Koros, *J. Memb. Sci.,* 2008, **314,** 193–199.

10 C. Zhang, Y. Dai, J. R. Johnson, O. Karvan, and W. J. Koros, *J. Memb. Sci.,* 2012, **389,** 34–42.

11 D. Bastani, N. Esmaeili, and M. Asadollahi, J. *Ind. Eng. Chem.,* 2013, **19,** 375–393.

12 D. Q. Vu, W. J. Koros, and S. J. Miller, *J. Memb. Sci.,* 2003, **211,** 311–334.

13 T. T. Moore and W. J. Koros, *J. Mol. Struct.,* 2005, **739,** 87–98.

14 H. B. Tanh Jeazet, C. Staudt, and C. Janiak, *Dalton Trans.,* 2012, **41,** 14003–140027.

15 P. S. Goh, A. F. Ismail, S. M. Sanip, B. C. Ng, and M. Aziz, *Sep. Purif. Technol.,* 2011, **81,** 243–264.

16 B. Zornoza, C. Tellez, J. Coronas, J. Gascon, and F. Kapteijn, *Microporous Mesoporous Mater.,* 2013, **166,** 67–78.

17 J.-R. Li, J. Sculley, and H.-C. Zhou, *Chem. Rev.,* 2012, **112,** 869–932.

18 U. Mueller, M. Schubert, F. Teich, H. Puetter, K. Schierle-Arndt, and J. Pastré, *J. Mater. Chem.,* 2006, **16,** 626-636.

19 S. R. Venna and M. A. Carreon, *J. Am. Chem. Soc.,* 2010, **132,** 76–78.

20 H. Deng, C. J. Doonan, H. Furukawa, R. B. Ferreira, J. Towne, C. B. Knobler, B. Wang, and O. M. Yaghi, *Science,* 2010, **327,** 846–850.

21 S. R. Caskey, A. G. Wong-Foy, and A. J. Matzger, *J. Am. Chem. Soc.,* 2008, **130,** 10870–10871.

22 K. K. Tanabe and S. M. Cohen, *Chem. Soc. Rev.,* 2011, **40,** 498–519.

23 M. Eddaoudi, J. Kim, N. Rosi, D. Vodak, J. Wachter, M. O'Keeffe, and O. M. Yaghi, *Science,* 2002, **295,** 469–472.

24 T. Li, D.-L. Chen, J. E. Sullivan, M. T. Kozlowski, J. K. Johnson, and N. L. Rosi, *Chem. Sci.,* 2013, **4,** 1746-1755.

25 S. Basu, A. Cano-Odena, and I. F. J. Vankelecom, *J. Memb. Sci.,* 2010, **362,** 478–487.

26 X. Y. Chen, H. Vinh-Thang, D. Rodrigue, and S. Kaliaguine, *Ind. Eng. Chem. Res.,* 2012, **51,** 6895–6906.

27 Y. Li, T. Chung, C. Cao, and S. Kulprathipana, *J. Memb. Sci.,* 2005, **260,** 45–55.

28 M. J. C. Ordoñez, K. J. Balkus, J. P. Ferraris, and I. H. Musselman, *J. Memb. Sci.,* 2010, **361,** 28–37.

29 E. V. Perez, K. J. Balkus, J. P. Ferraris, and I. H. Musselman, *J. Memb. Sci.,* 2009, **328,** 165–173.

30 T. Rodenas, M. van Dalen, E. García-Pérez, P. Serra-Crespo, B. Zornoza, F. Kapteijn, and J. Gascon, *Adv. Funct. Mater.,* 2014, **24,** 268–268.

31 Q. Song, S. K. Nataraj, M. V. Roussenova, J. C. Tan, D. J. Hughes, W. Li, P. Bourgoin, M. A. Alam, A. K. Cheetham, S. A. Al-Muhtaseb, and E. Sivaniah, *Energy Environ. Sci.,* 2012, **5,** 8359-8369.

32 B. Zornoza, B. Seoane, J.M. Zornaro, C. Tellez, J. Coronas, *ChemPhysChem*, 2011, **12,** 2781-2785.

33 S. J. Garibay and S. M. Cohen, *Chem. Commun. (Camb).,* 2010, **46,** 7700–7702

34 S. Biswas and P. Van Der Voort, Eur. *J. Inorg. Chem.,* 2013, **2013 (12),** 2154–2160.

35 C. H. Lau, R. Babarao, and M. R. Hill, *Chem. Commun. (Camb).,* 2013, **49,** 3634–3636.

36 J. H. Cavka, S. Jakobsen, U. Olsbye, N. Guillou, C. Lamberti, S. Bordiga, and K. P. Lillerud, *J. Am. Chem. Soc.,* 2008, **130,** 13850–13851.

37 Q. Yang, A. D. Wiersum, H. Jobic, V. Guillerm, C. Serre, P. L. Llewellyn, and G. Maurin, *J. Phys. Chem. C,* 2011, **115,** 13768–13774.

38 G. E. Cmarik, M. Kim, S. M. Cohen, and K. S. Walton, *Langmuir,* 2012, **28,** 15606–15613.

39 C. Zlotea, D. Phanon, M. Mazaj, D. Heurtaux, V. Guillerm, C. Serre, P. Horcajada, T. Devic, E. Magnier, F. Cuevas, G. Férey, P. L. Llewellyn, and M. Latroche, *Dalton Trans.,* 2011, **40,** 4879–4881.

40 H. Jasuja, J. Zang, D. S. Sholl, and K. S. Walton, *J. Phys. Chem. C,* 2012, **116,** 23526–23532.

41 R. Mahajan and W. J. Koros, *Polym. Eng. Sci.,* 2002, **42,** 1432–1441.

42 R. Mahajan and W. J. Koros, *Polym. Eng. Sci.,* 2002, **42,** 1420–1431.

43 A. Schaate, P. Roy, A. Godt, J. Lippke, F. Waltz, M. Wiebcke, and P. Behrens, *Chemistry,* 2011, **17,** 6643–6651.

44 M. Alexandre and P. Dubois, *Mater. Sci. Eng. R Reports,* 2000, **28,** 1–63.

45 J. Ahn, W.-J. Chung, I. Pinnau, and M. D. Guiver, *J. Memb. Sci.,* 2008, **314,** 123–133.

46 T. Pechar, S. Kim, B. Vaughan, E. Marand, M. Tsapatsis, H. Jeong, and C. Cornelius, *J. Memb. Sci.,* 2006, *277,* 195–202.

47 Y. Li, W. B. Krantz, and T.-S. Chung, *AIChE J.,* 2007, **53,** 2470–2475.

48 M. Q. Zhang, M. Z. Rong, H. B. Zhang, and K. Friedrich, *Polym. Eng. Sci.,* 2003, **43,** 490–500.

49 M. Z. Rong, M. Q. Zhang, Y. X. Zheng, H. M. Zeng, R. Walter, and K. Friedrich, *Polymer (Guildf).,* 2001, **42,** 167–183.

50 A. F. Bushell, M. P. Attfield, C. R. Mason, P. M. Budd, Y. Yampolskii, L. Starannikova, A. Rebrov, F. Bazzarelli, P. Bernardo, J. Carolus Jansen, M. Lanč, K. Friess, V. Shantarovich, V. Gustov, and V. Isaeva, *J. Memb. Sci.,* 2013, **427,** 48–62.

Table of Contents and Graphical Abstract

High quality mixed matrix membranes are fabricated by dispersing surface functionalized MOF particles in Matrimid polymer. An improved polymer-particle interface is achieved by engineering the surface of the MOF particles. The resultant mixed matrix membranes have 3 times higher CO_2 permeability compared to the pure Matrimid membranes with ~25% improvement in CO_2/N_2 selectivity.

S. R. Venna[1,2], M. Lartey[1,6], T. Li[3], A. Spore[3], S. Kumar[1,6], H. B. Nulwala[1,4], D. R. Luebke[1], N. L. Rosi[3,*], E. Albenze[1,5,*]

Fabrication of MMMs with improved gas separation properties using externally-functionalized MOF particles